ELSEVIER

Contents lists available at ScienceDirect

Earth and Planetary Science Letters

www.elsevier.com/locate/epsl



How the energy budget scales from the laboratory to the crust in accretionary wedges



Jessica McBeck^{a,*}, Michele Cooke^b, François Renard^{a,c}

- ^a Physics of Geological Processes, The Njord Centre, Department of Geosciences, University of Oslo, Norway
- ^b Department of Geosciences, University of Massachusetts Amherst, MA, USA
- ^c University Grenoble Alpes, University Savoie Mont Blanc, CNRS, IRD, IFSTTAR, ISTerre, 38000 Grenoble, France

ARTICLE INFO

Article history: Received 12 November 2019 Received in revised form 10 April 2020 Accepted 12 April 2020 Available online xxxx Editor: R. Bendick

Keywords: scaling energy budget accretionary prisms physical analog experiments

ABSTRACT

We investigate the scaling properties of the mechanical energy budget in accretionary prisms across five orders of magnitude, from the laboratory centimeter-scale to crustal kilometer-scale. We first develop numerical models that match the length scale, fault and material properties, surface topography, and fault geometries observed in scaled dry sand accretionary experiments. As we systematically increase the spatial dimensions of the numerical models by orders of magnitude, we calculate each component of the energy budget both before and after the first thrust fault pair develops. The increase of both the bulk stiffness and slip weakening distance from the laboratory- to crustal-scale produces a scale-invariant partitioning of the energy budget, relative to the total work done on the system. The components scale as power laws with exponents of three. Consequently, accurate laboratory simulations of the energetics of deformation within crustal accretionary wedges require careful scaling of the stiffness and slip weakening distance. Preceding thrust fault development at both the laboratory and crustal scale, the internal work consumes the largest portion of the budget (67-77%) and frictional work consumes the next largest portion (17-27%), Following thrusting, frictional work and internal work consume similar portions of the energy budget (38-50%). The sum of the remaining energy budget components, including gravitational work, seismic work, and the work of fracture propagation, consume <10-15% of the total energy budget preceding and following thrust fault development.

© 2020 Published by Elsevier B.V.

1. Introduction

A critical question in the geophysical community is how to extend observations and measurements made in experiments at the laboratory-scale to physical phenomena in the Earth's crust at the kilometer-scale (e.g., **Fig.** 1). The energy budget provides a concise framework with which to quantify diverse deformational processes in both the laboratory and crust. This framework enables quantitative comparison of the varying energetic importance of interacting mechanical processes such as uplift against gravity, frictional sliding, and off-fault deformation (e.g., Cooke and Madden, 2014).

In recent years, advances in field techniques and the quantitative monitoring of experiments have provided estimates of components of the deformational energy budget at a range of scales (Fulton et al., 2013; Savage et al., 2014; Herbert et al., 2015; Passelègue et al., 2016; McBeck et al., 2018, 2019; Coffey et al.,

* Corresponding author.

E-mail address: j.a.mcbeck@geo.uio.no (J. McBeck).

2019; Aben et al., 2019). Laboratory experiments have constrained several components of the energy budget at fine temporal resolution as faults slip and propagate, including the work of uplift against gravity, W_{grav} , the work done against frictional sliding, W_{fric} , the work of off-fault internal deformation, W_{int} , the work of fault propagation (i.e., fracture energy), W_{prop} , the work done in radiated seismic energy, W_{seis} , and the total external work, W_{ext} (e.g., Herbert et al., 2015; Passelègue et al., 2016; McBeck et al., 2018, 2019; Aben et al., 2019). In contrast, field observations have yielded estimates of a few components of the energy budget, and typically only one component in a given tectonic environment at one particular moment in time (e.g., Ismat, 2009; Meade, 2013; Fulton et al., 2013; Savage et al., 2014; Coffey et al., 2019). Whereas field observations have not yet been able to estimate the overall system efficiency, the total external work applied to the system, W_{ext} , laboratory experiments enable estimates of the temporal evolution of W_{ext} as faults slip, propagate and interact. With displacement loading conditions, lower external tractions produce lower W_{ext} , and thus signal more efficient fault systems. The total external work expended on a deforming system may be

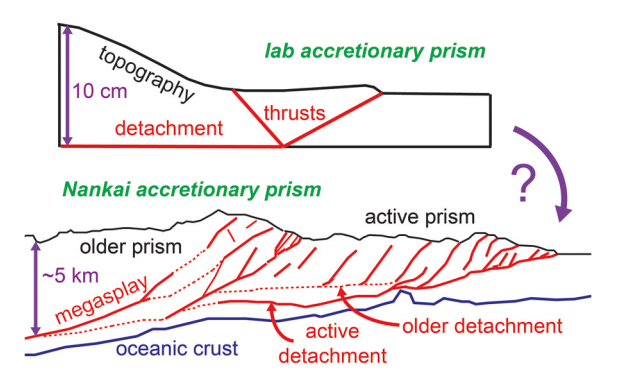


Fig. 1. Schematic representation of the cross-section of an accretionary wedge observed in the laboratory (upper), and observed in the crust (lower). Black lines indicate the topography and boundaries of the wedges. Red lines indicate the active and inactive faults, including the basal detachment and thrust faults. Lower sketch follows from interpretations of the NanTroSEIZE seismic transect (Strasser et al., 2009). (For interpretation of the colors in the figure(s), the reader is referred to the web version of this article.)

the most important element of the energy budget because numerical and laboratory work suggests that it can yield accurate predictions of fault growth (McBeck et al., 2016, 2017a, 2017b; Madden et al., 2017). Laboratory and numerical analyses that estimate all the components of the energy budget find that frictional work dominates the energy budget in diverse systems, such as during thrust fault propagation in accretionary wedges composed of sand (McBeck et al., 2018), slip along pre-cut faults in crystalline rock (McBeck et al., 2019), fracture coalescence in initially intact crystalline rock (Aben et al., 2019), and dynamic earthquake rupture (Okubo et al., 2019).

If frictional work dominates the energy budget at the crustal scale, then field analyses may only need to evaluate the frictional work expended within the system in order to estimate the overall system efficiency, and thus predict fault evolution (e.g., Madden et al., 2017). However, the scaling of the work budget components remains uncertain. The gap in robust estimates of the overall system efficiency and other energy budget components at the field scale (e.g., Coffey et al., 2019), and the growing number of data points at the laboratory scale (e.g., Aben et al., 2019), provide incentive to identify the length scaling relationships of components of the deformational energy budget.

Here, we examine the scaling relationships of the components of the energy budget using numerical models of accretionary wedges across a range of scales. The cm-scale accretionary models match the geometry and physical properties of dry sand wedges built and deformed at the University of Cergy Pointoise (UCP) (e.g., McBeck et al., 2018). The accretion experiments performed at UCP provide fine spatial and temporal resolution observations of fault development and off-fault deformation, thereby enabling robust benchmarking of the laboratory-scaled numerical models. Furthermore, because McBeck et al. (2018) estimated the evolving components of the energy budget from observations of the experiments performed at UCP, we may directly compare the energy budget partitioning within the numerical models developed here to the experimental results. The larger scale models of this study use the same accretionary system geometry and differing material properties, as appropriate (e.g., Hubbert, 1937). By constraining the scaling relationships between the energy budget components and the size of the deformation system, we aim to provide a quantitative method of linking observations of the energy budget at the laboratory scale to those at the crustal scale.

Deformation within dry sand laboratory wedges simulates crustal accretionary processes because the cohesion of the dry sand is chosen to scale to the inherent shear strength of the crust via the difference in length scale between the two systems

(e.g., Hubbert, 1937; Ritter et al., 2016). This careful scaling of the analog material allows the processes observed within laboratory experiments to accurately simulate crustal deformational processes (e.g., Reber et al., 2020). The material properties along and around faults control the partitioning of the deformational energy budget of fault systems. While the friction and cohesion/strength control the onset and orientation of faulting, other material properties, such as the effective bulk stiffness and the slip weakening distance, play a role in the partitioning of deformation on and off of faults, and thus the energy budget. The friction coefficients are similar for the analog material (sand) and crustal material (Lohrmann et al., 2003; Klinkmüller et al., 2016). However, evidence suggests that the bulk stiffness and slip-weakening distance depend on the length scale of the system, even in systems composed of the same material (Bieniawski, 1984; Marone and Kilgore, 1993; Ritter et al., 2016). So, differences in the material properties of the laboratory prisms and crustal prisms arise from differences in the length scale as well as differences in the deforming material. Here, we utilize laboratory measurements of sand and rock properties to scale the effective stiffness and slip-weakening distance with length in the numerical accretion models.

Our numerical analysis shows that when the material properties of bulk stiffness and slip-weakening distance increase with the length scale as power laws with exponents of 0.8-1, the components of the energy budget scale with the length scale as power laws with exponents of three over five orders of magnitude. When the scaling of these two material properties has an exponent of one, each work budget component consumes a constant percentage of the total work from the laboratory scale to the crustal scale. When the scaling of the material properties has an exponent of less than one, these percentages vary from the laboratory to crustal scale. Despite these variations, the work components have similar rankings: scaling the material properties with the length scale as power laws with exponents of 0.8-1 produces energy budget partitioning of $W_{int} > W_{fric} >> W_{grav} \approx W_{seis}$ preceding thrust fault development, and $W_{int} \approx W_{fric} >> W_{grav} \approx W_{prop} \approx W_{seis}$, following thrust fault development in accretionary wedges.

2. Background

2.1. Energy budget

Here, we describe the physical properties that produce the energy budget components, and thus how material properties may vary the energy budget partitioning. The complete mechanical energy budget of upper crustal fault systems includes W_{grav} , W_{fric} , W_{int} , W_{prop} , and W_{seis} , such that $W_{grav} + W_{fric} + W_{int} + W_{prop} + W_{seis}$ is equal to the total external work, W_{ext} (e.g., Cooke and Madden, 2014). This conceptualization considers deformation within the upper crust and does not consider energy dissipated in plastic processes. Previous work provides the derivations for each component of the energy budget (e.g., Cooke and Madden, 2014). **Text** S1 lists the equations of each component.

The external work, W_{ext} , is a product of the tractions and displacements acting on the model boundaries. When the loading is applied incrementally to a system, we must calculate W_{ext} and all the work budget components by integrating them over the applied loading steps. Under displacement loading conditions, W_{ext} only varies with the tractions that arise on the external boundaries. Increasing the model stiffness thus increases W_{ext} by increasing the tractions required to achieve the prescribed boundary displacements.

During slip, fault strength evolves from an initial static strength to a typically weaker sliding strength over the slip-weakening distance, D_c . This change in strength produces energy available for W_{prop} or W_{seis} (e.g., Figure 2 of Cooke and Madden, 2014). The

partitioning of energy into W_{prop} and W_{seis} depends on the energetic reference frame. While seismologists may partition the energy budget differently than geologists (e.g., Kanamori and Heaton, 2000; Savage and Cooke, 2010), this partitioning is conceptual as we lack detailed earthquake source data to validate either conceptualization. Here, we follow Cooke and Madden (2014) and consider that where (and when) the slip on the fault, s, is less than D_c , greater energy is spent to create new local fractures, W_{prop} , than to generate seismic waves, W_{seis} . Where and when $s > D_c$, no additional local fractures are produced, and W_{seis} consumes the energy produced by the change in fault strength (**Text** S1). Changing D_c thus influences the energy budget by changing the partitioning of W_{prop} and W_{seis} .

The frictional work, W_{fric} , is a product of the sliding shear tractions and slip integrated along all the faults (**Text** S1). In one loading step, W_{fric} equals the sum of the new fault slip in that loading step multiplied by the sliding shear stress on each fault element. The gravitational work, W_{grav} , is the product of the vertical uplift within the system and the overburden weight (i.e., density multiplied by the gravitational constant) integrated across the model (**Text** S1).

2.2. Effective stiffness of laboratory and crustal accretionary wedges

We design the numerical models at the centimeter-scale to match the laboratory physical experiments, and so we use the material properties of the analog material (dry sand) for the centimeter-scale models. For the models at the kilometer-scale, we use a range of values that matches estimates for the material that comprises crustal prisms. Then, using the values at the centimeter-and kilometer-scale, we interpolate a relationship between the material properties at these two length scales in order to identify the appropriate material properties for hypothetical models of intermediate scale between the centimeter- and kilometer-scales.

The sand deposition system at UCP constructs homogeneous accretionary prisms with planar grain alignment (Maillot, 2013). The density and planarity of the sandpacks influence the effective elastic modulus by controlling the magnitude of compaction that the wedge accommodates preceding localized thrust faulting. McBeck et al. (2018) measured an effective stiffness of 1 MPa for the UCP wedges using normal force gauges and the displacement field of the sandpack estimated via digital image correlation of photos. Consequently, the centimeter-scale numerical models in the present work use elastic moduli of 1 MPa, matching that of the UCP experiments.

Estimates of the effective elastic modulus of consolidated sedimentary rocks that may comprise crustal accretionary prisms, such as sandstone, shale and brine-saturated mudrock are within the range of 20-90 GPa (Mondol et al., 2007; Sone and Zoback, 2013; Fjær and Nes, 2014). Material recovered from shallow cores of crustal accretionary wedges tend to have lower stiffness of ~1-10 GPa (e.g., Spinelli et al., 2007; Raimbourg et al., 2011) than those of consolidated sedimentary rocks. Numerical models of crustal accretionary wedges prescribe Young's moduli within the lower range (6 GPa, Hardy and Finch, 2006). **Text** S2 describes additional complexities of the spatially varying effective stiffness within crustal accretionary wedges.

Due to the range in estimates of the effective stiffness of accretionary wedges, we examine energy budget partitioning in kilometer-scale models with elastic moduli, E, of both 10 GPa and 100 GPa. The lower range (10 GPa) agrees with estimates from shallow core material, while the upper range (100 GPa) agrees with estimates from sedimentary rock that may comprise accretionary wedges (e.g., Spinelli et al., 2007; Mondol et al., 2007). With E=10 GPa at the kilometer-scale (length scale $E=10^{5}$), we may choose a power law interpolation between the length scale of

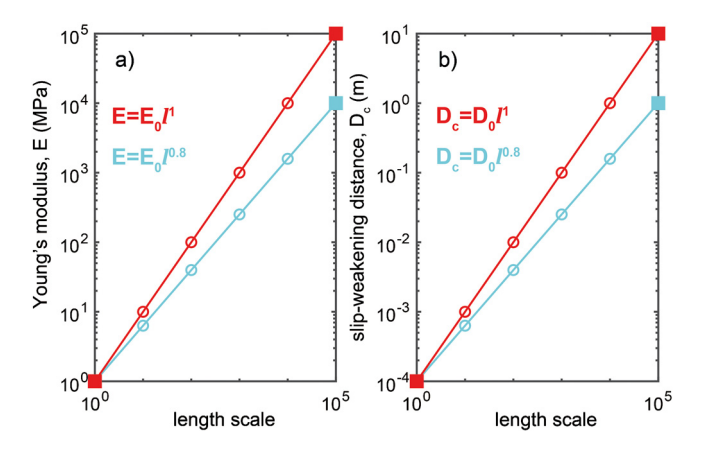


Fig. 2. Relationship between the length scale and Young's modulus, E, (a) and slipweakening distance, D_c , (b) derived from upper (red) and lower (blue) estimates of crustal material properties. Estimates of the laboratory-scale material properties (E=1 MPa, D_c =0.1 mm) constrain the relationship between length scale and property at the smallest length scale. Estimates of the crustal-scale material properties (E=10-100 GPa, D_c =1-10 m) constrain the relationships at the crustal length scale (10^{5}). Deriving the power-law relationships between the laboratory-scale properties and the two crustal-scale estimates (squares) produce power law exponents of 0.8 and 1, and the appropriate values to use at length scales from 10^{1} - 10^{4} (circles) for E (MPa) and D_c (m).

the system, l, and the effective elastic modulus (**Fig. 2**). Interpolating between the laboratory stiffness, E_0 , (1 MPa) and lower estimate of crustal E (10⁴ MPa) produces the relationship $E=E_0l^{0.8}$. Using the upper estimate of the crustal E (10⁵ MPa), this interpolation produces the relationship $E=E_0l^{1}$. These two interpolations produce two sets of effective elastic moduli that span 10-100 GPa at the crustal scale (**Fig. 2**).

2.3. Slip-weakening distance of laboratory and crustal faults

The slip-weakening distance is the distance over which the frictional strength evolves from a static to dynamic value on fault surfaces, D_c . For faults in rock, D_c is related to the sliding velocity, shear stress drop, and material properties (e.g., Cocco and Bizzarri, 2002). For faults in dry sand, the diameter of sand grains is thought to control the slip-weakening distance. The reactivation of slip in ring-shear tests of dry sand provide estimates of this distance (0.1-1 mm) (Panien et al., 2006; Klinkmüller et al., 2016). The median grain diameter of the CV32 sand used in these experiments is 250 μ m (Maillot, 2013), and so we consider 0.1 mm as D_c in the centimeter-scale models.

Laboratory and geophysical evidence suggest that D_c depends on the scale of the system and thus the cumulative slip on the fault (e.g., Marone and Kilgore, 1993). This distance ranges from micrometers measured at the laboratory scale to meters estimated from earthquake parameters (Dieterich, 1981; Ohnaka and Kuwahara, 1990; Mikumo et al., 2003; Di Toro et al., 2004; Hirose and Bystricky, 2007). The discrepancy between laboratory and crustal estimates has prompted the suggestion that D_c is a scale-dependent property, which may depend on the roughness of fault surfaces, the thickness of fault gouge, the width of the fault zone, the particle size of gouge, the accumulated shear strain, and/or the total slip on the fault (e.g., Marone and Kilgore, 1993; Ohnaka, 2000; Pulido and Irikura, 2000; Guatteri et al., 2001; Abercrombie and Rice, 2005; Cocco and Tinti, 2008; Tinti et al., 2009).

Due to the range in estimates of D_c in crustal faults, we examine energy budget partitioning in kilometer-scale models with slipweakening distances, D_c , of 1 m and 10 m. This range agrees with geophysical estimates of D_c (e.g., Mikumo et al., 2003). Interpolating D_c between that at the centimeter-scale, D_0 =0.1 mm, and the end-members at the kilometer-scale, 1 m < D_c < 10 m, pro-

duces relationships between the length scale and D_c as $D_c = D_0 l^{0.8}$ or $D_c = D_0 l^{1}$ (**Fig. 2**). The exponents of the relationships between the length scale, and D_c and E match, but not by design. The exponents arise from the estimates of the centimeter- and kilometer-scale values derived from previous independent measurements.

Following this approach of scaling E and D_c with the length scale of the system, we examine the partitioning of the energy budget in accretionary wedges. We calculate this partitioning in simulations that represent the wedge both before and after accretionary thrust faults develop. With the models at the laboratory scale, we use the set of material properties derived from laboratory measurements of the analog material. For models at the crustal scale, we develop two sets of numerical wedges using the lower and upper bounds of material properties described above (E=10 and 100 GPa, D_c =1 and 10 m for the crustal scales). For models between the laboratory and crustal scale, we use the end-member relationships of p= $p_0 l^{0.8}$ and p= $p_0 l^{1}$, to estimate the value of the property at the hypothetical intermediate scales, p, from the laboratory-scale property, p_0 .

3. Methods

3.1. Fric2D numerical model

To constrain the energy budget, we use the 2D plane-strain linear elastic boundary element method code Fric2D (Cooke and Pollard, 1997). In these 2D models, systems are considered to be one-meter thick in- and out- of the plane (z-direction), where the y-axis is vertical and the x-axis is horizontal. Consequently, increasing the length scale of the models involves increasing the cross-sectional area of the models, but not the thickness in the z-direction.

In the boundary element method implementation, fractures and boundaries are composed of linear elements of (ideally) equal length that may open or slip, but not interpenetrate, due to the applied loading or slip/opening along other elements. Fric2D solves the displacement-discontinuity equations, producing a set of normal and shear displacements and tractions on each element, including the fractures and external boundaries of the systems. Fric2D also solves for the displacements and stress tensors at any point throughout the system, i.e., the nominally intact off-fault material. The off-fault material is homogeneous and isotropic, so one set of elastic parameters is prescribed, including the Young's modulus and Poisson's ratio.

Fracture elements may fail either in tension or shear. Elements fail in tension and subsequently open when the normal stress on the element exceeds the tensile strength, with the adopted tension positive sign convention. Fracture elements fail in shear and then slip following the Coulomb failure criterion. Fric2D captures slipweakening behavior such that the effective friction evolves linearly from a static to dynamic value over a prescribed $D_{\rm c}$ (Savage and Cooke, 2010).

3.2. Model design

The fault geometry and surface topography of the models are designed to match laboratory experiments performed at UCP, which are 50 cm long and 9.5 cm tall (**Fig.** 3). We apply 0.5 cm of backwall normal displacement, u_n , to simulate the horizontal contraction of the wedge in the laboratory-scale models. This loading promotes slip along through-going thrust faults in these models. The crustal scale models (length scale of 10^5) have dimensions (50 km long and 9.5 km tall), u_n (0.5 km), and element lengths (1 km) that are 10^5 times those of the laboratory scale models (length scale of 10^0) (**Fig.** 3). In all models, the bottom and right sides of the model are fixed, and thus may experience normal and shear

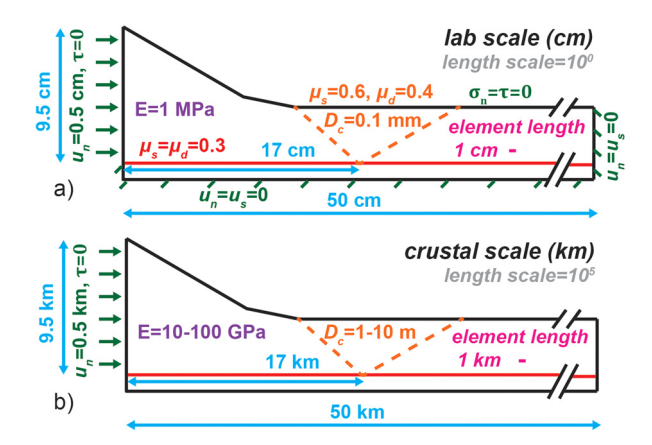


Fig. 3. Schematic of model set up at the laboratory scale of centimeters (a), and crustal scale of kilometers (b). The laboratory scale models match the dimensions, material and fault properties, and fault geometry observed in physical laboratory experiments. Increasing the length scale includes increasing the model dimensions (blue), the applied backwall displacement (green) and element length (pink). The frictional strength of the thrust faults (orange) evolves linearly with slip over D_c from a static (μ_s =0.6) to dynamic (μ_d =0.4) friction coefficient. The basal detachment (red) has a constant friction coefficient of 0.3. We derive the position and dips of the thrust faults from observations of the physical experiments of McBeck et al. (2018). The scale-variant material properties, Young's modulus, E, and slipweakening distance, D_c , increase with the length scale.

tractions. The top of the model is allowed to deform without experiencing normal or shear tractions.

The material properties used in the models that do not vary by orders of magnitude between laboratory and crustal scale (friction coefficients, fault cohesion, density) have the same values in all of the models. The frictional properties of basal detachment faults between sand and glass, and thrust faults within sand are wellcharacterized (Lohrmann et al., 2003; Maillot, 2013; Klinkmüller et al., 2016). In the numerical models, the effective friction coefficient of the detachment fault does not evolve with slip, and remains constant at 0.3. The effective friction coefficient of the thrust faults evolves linearly with slip over D_c from the static (0.6) to dynamic (0.4) friction value. We prescribe a density of 1.7 g/cm³ that matches measurements of sand aggregates produced at UCP (Maillot, 2013), which is at the same order of magnitude obtained of values for poorly lithified sediments found at shallow depths within accretionary prisms (e.g., Mondol et al., 2007). The consistency of the density and friction coefficients ensures that the difference in the strengths between the laboratory and numerical models only arise from the length scale.

We calculate the components of the energy budget in models that represent the wedge before and after the first thrust-fault pair develops. We synthesize observations from the physical experiments (McBeck et al., 2018) to develop a representative fault geometry (dips and positions) for the pair of thrust faults (Fig. 3). Incrementing the applied normal displacement to the backwall with 100 loading steps provides a compromise between run time and calculation accuracy (e.g., Figure S1). To maximize resolution of the results, we use the smallest appropriate element length in boundary element method models (Text S3).

4. Results

4.1. Energy budget partitioning at the laboratory scale

Preceding thrust fault development in the laboratory scale models, W_{fric} consumes 17% of W_{ext} , while W_{grav} consumes 1%, and W_{seis} consumes 4% (**Fig.** 4). W_{prop} does not consume any work preceding thrust fault development because the effective friction of the detachment does not evolve with slip. Following thrust

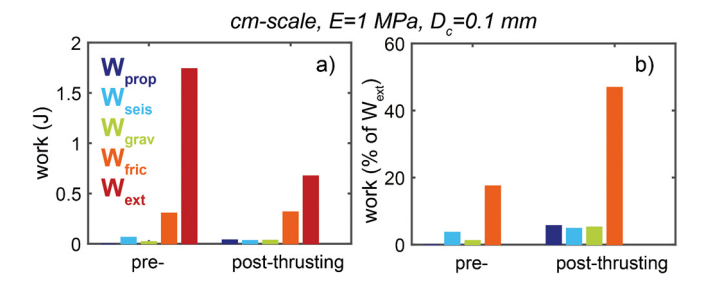


Fig. 4. Work budget of the wedges at the centimeter-scale (scaling factor= 10^0) before (pre-thrusting) and after (post-thrusting) thrust fault development. Energy budget is shown as the magnitude of work consumed pre- and post-thrusting (a) and as percentages of each component out of the total external work, W_{ext} (b). Work of fault propagation, W_{prop} , seismic work, W_{seis} , gravitational work, W_{grav} , frictional work, W_{fric} , and W_{ext} shown with dark blue, light blue, green, orange and red, respectively.

fault development, the wedge consumes less W_{ext} and more W_{seis} , W_{prop} , W_{grav} , and W_{fric} than the wedge preceding thrust fault development (**Fig.** 4). This partitioning of the energy budget matches the partitioning estimated from the physical experiments (McBeck et al., 2018) from which we designed the numerical models. In both systems, thrust fault development increases W_{grav} and W_{fric} , and decreases W_{ext} . This evolution arises because thrust faulting reduces the internal work, W_{int} , stored in the material around the fault. W_{int} thus provides the energy used in the production of new fault surfaces.

The similarities of the energy budget partitioning pre- and postthrusting in the experimental and numerical wedges arise from the similarity of the physical processes acting within these wedges. We focus on this idea by comparing the 2D incremental displacement fields and fault slip distribution in the physical and numerical wedges. Digital image correlation of pairs of sequential photographs taken through the glass sidewalls of the physical experiments (McBeck et al., 2018) reveal the incremental displacement field, from which we calculate the incremental strain components (Fig. 5a-b). Correspondingly, we set up the numerical models to produce incremental displacement fields rather than the cumulative displacements so that we can directly compare the numerical results to the experimental observations. Fig. 5 compares the incremental displacement and slip in the numerical models and an early stage of the laboratory experiments, such that the applied displacement is similar for both systems. In the laboratory experiments, thrust faulting produces a zone of uplift between the thrust faults (Fig. 5a), similar to the laboratory scale numerical models (Fig. 5c). In both the experiments and numerical models, the forethrust hosts higher incremental shear strain (and thus slip) than the backthrust. In addition, in both systems the detachment fault hosts higher incremental shear strain and slip along its length between the backthrust root and the backwall than either of the thrusts. The similarities between the energy budget partitioning, and kinematics in the physical and numerical wedges at the laboratory scale indicate that the laboratory-scale numerical models reproduce the relevant physics of the laboratory experiments.

4.2. Energy budget partitioning across five orders of magnitude of length scale

We compare the energy budget of wedges with length scales that range from centimeters (length scale, l= 10^0) to kilometers (l= 10^5). We report the energy budget in simulations with varying length scales with three methods: the value of each work component in log-log space, the value of each component divided by the cube of the length scale, l³, and the percentage of the total external work, W_{ext} , that each of the work components consumes (**Fig.** 6). Over five orders of magnitude of length scale, each work

component increases approximately as power-laws with exponents of three, for wedges both pre- and post-thrusting (**Fig.** 6a). Consequently, the value of the work component divided by l^3 highlights the deviations from this power law scaling with differing length scales. The percentage of W_{ext} that each component consumes shows how the partitioning of the energy budget evolves with length scale.

The vertical bars in **Fig.** 6 show the ranges produced by the upper and lower estimates of the material properties at each length scale (e.g., **Fig.** 2). When we apply the upper estimates of the effective E and D_c , at the kilometer-scale E=100 GPa and D_c =10 m, then the property, p, scales as $p = p_0 l^1$. When we apply the lower estimates of these properties, at the kilometer-scale E=10 GPa and D_c =1 m, then $p = p_0 l^{0.8}$.

Using the upper material scaling estimates, the work components divided by I^3 and the percentage that each work component consumes are constant from the centimeter- to kilometer-scale models (**Figs.** 6, S2). Using the lower material scaling estimates, the energy budget partitioning varies across the length scales (**Figs.** 6, S2). The variation produced by the lower estimates arises from the impact of E and D_C on W_{ext} , W_{seis} and W_{prop} . Under the same applied displacement, stiffer wedges develop larger W_{ext} than softer wedges due to the larger boundary tractions. Stiffer wedges may also help localize deformation (slip) onto faults from the off-fault volume, thereby increasing W_{fric} (**Fig.** 6c). The D_C controls the partitioning of W_{seis} and W_{prop} (**Text** S1). Smaller D_C relative to slip on a fault segment, will tend to partition work toward W_{prop} and away from W_{seis} (**Fig.** 6b-c). In the endmember case when D_C =0, then W_{seis} =0.

For these models, varying the material properties influence each energy budget component to different degrees (Fig. 6). Preceding thrust faulting development, W_{grav}/l^3 and W_{fric}/l^3 do not change by significant magnitudes from the 100 to 105 length scales. In contrast, W_{seis}/l^3 and W_{ext}/l^3 both decrease with increasing length scale. The scale-dependence of the work budget components produces moderately differing partitioning of the energy budget at the centimeter- and kilometer-scales. At the centimeterscale preceding thrusting, the relative portion of W_{ext} for each work budget components is: W_{fric} (27%) > W_{seis} (3.7%) > W_{grav} (1.2%). At the kilometer-scale preceding thrusting, W_{fric} (17-27%) $> W_{grav}$ (1.2-3.7%) $\approx W_{seis}$ (1.3-3.6%). Following thrusting at the centimeter-scale, the relative portion of W_{ext} for each work components is: W_{fric} (47%) > W_{prop} (5.7%) $\approx W_{grav}$ (5.2%) $\approx W_{seis}$ (4.8%). Following thrust fault development at the kilometer-scale, W_{fric} (39-47%) > W_{grav} (5.2-5.5%) $\approx W_{prop}$ (3-5.4%) $\approx W_{seis}$ (3-4.7%). Thus, the importance of W_{grav} , W_{prop} , and W_{seis} varies across the length scales using the lower estimate of material properties. However, W_{fric} consistently dominates the budget preceding and following thrusting as Wgrav, Wprop and Wseis change in their ranking of importance.

To further examine the consequence of varying ranges of material properties on energy budget partitioning at the centimeterand kilometer-scales, we report the difference in the percentage of W_{ext} that each component consumes at the centimeter-scale, and at the kilometer-scale using the upper and lower estimates of material properties (**Fig.** 7). Because the difference between the percentage of each component at the centimeter- and kilometer-scale is near 10% for W_{fric} , and <3% for W_{prop} , W_{seis} , and W_{grav} , here we focus on understanding the physical processes producing the differences in W_{fric} .

Preceding thrusting, W_{fric} consumes more W_{ext} in the kilometer-scale model with the lower estimates of material properties (E=10 GPa, D_c =1 m) than the model with the upper estimates (E=100 GPa, D_c =10 m). The softer wedge consumes 27% W_{fric}/W_{ext} , and the stiffer wedge consumes 17% (**Figure** S2). The two wedges of kilometer-scale with different material properties

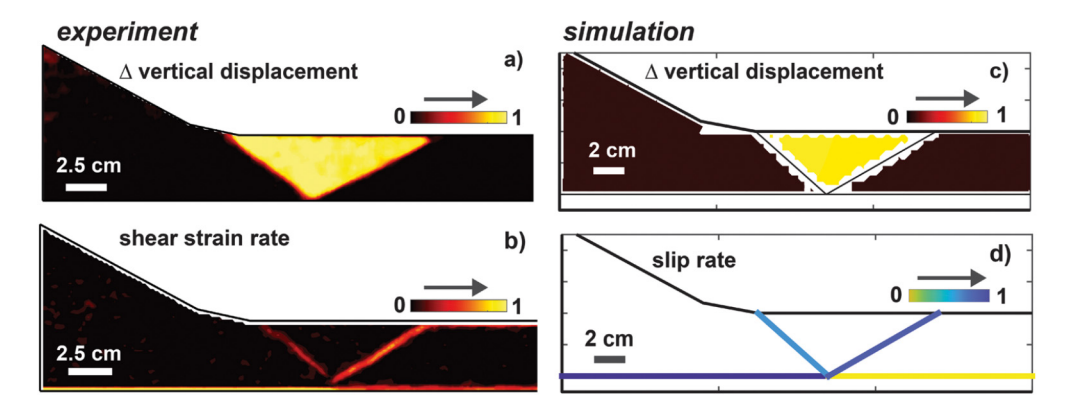


Fig. 5. Comparison of processes in physical analog laboratory experiments (left) and numerical models (right) at similar stages of backwall displacement. The incremental vertical displacement (a) and shear strain rate (b) of laboratory experiments were calculated from digital image correlation of sequential photographs of the wedge taken through the glass sidewall (McBeck et al., 2018). Incremental vertical displacement (c) and slip rate on faults (d) in numerical models that simulate the laboratory experiment. The spatial distribution of uplift and partitioning of slip among the faults are similar in the laboratory experiments and numerical models. The presented vertical displacement, shear strain and slip are normalized to their ranges in order to emphasize the spatial distribution of these parameters.

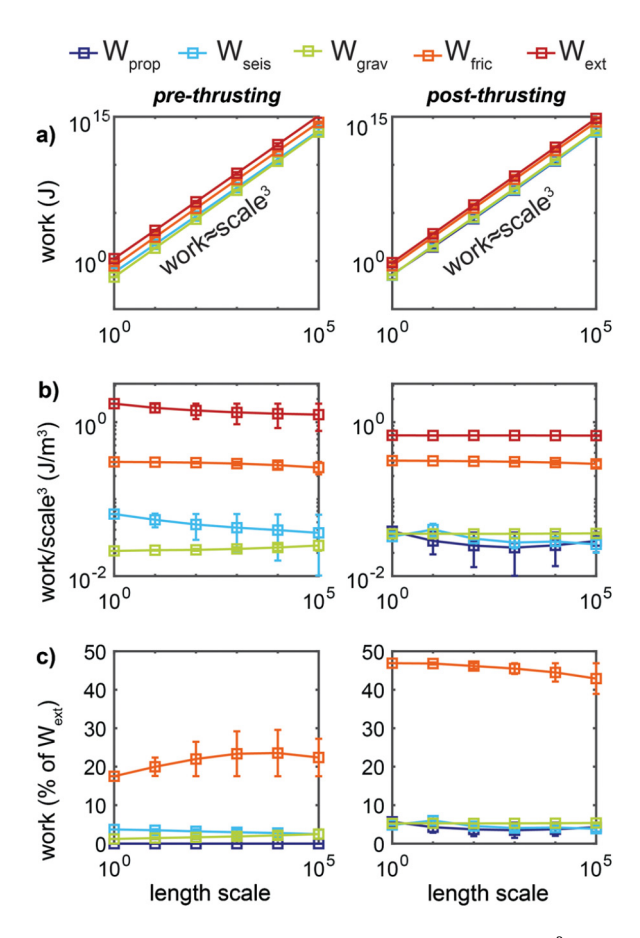


Fig. 6. Energy budget components in log-log space (a), as work/scale³ (b), and as percentages of the external work, W_{ext} (c). The vertical bars show the ranges in estimates produced by using different scaling relationships of the material properties. Figure S2 shows the work budget of these sets of models with the different scaling relationships separately. Components of the energy budget for wedges preceding thrusting and following thrusting shown on the left and right, respectively. a) The work components scale approximately as power laws with exponents of three. b) The work/scale³ shows the deviations of the work components from these power laws. If the material properties scale with the length as a power law with an exponent of 1, the partitioning of the energy budget is identical at the laboratory and crustal scale. If the material properties scale with an exponent of 0.8, the partitioning of the energy budget changes from the laboratory to crustal scale. W_{fric} consumes that largest portion of the energy budget both preceding and following thrust faulting at both scales, but the ranking of W_{prop} , W_{seis} and W_{grav} changes with scale. The sum of the percentages (c) does not reach 100% because we do not calculate the internal work, W_{int} .

produce similar detachment slip, and hence similar magnitudes of W_{fric} , so the difference in W_{fric}/W_{ext} arises from the change in W_{ext} with stiffness. Prior to thrust fault development, wedges with higher stiffness produce higher W_{ext} than softer wedges.

Following thrust fault development, we observe the opposite pattern of W_{fric}/W_{ext} than observed preceding faulting. When the thrust faults slip, the wedge with the upper estimates of material properties produces W_{fric}/W_{ext} (47%) greater than the wedge with the lower estimates (38%) (**Fig.** 7). The slip on the thrust faults reduces the impact of stiffness on W_{ext} . Rather than the stiffer wedge producing higher normal tractions along the backwall, the stiffer models produce greater slip along the thrust faults. Following thrust faulting, the W_{ext}/l^3 does not change significantly from the centimeter- to kilometer-scales (**Fig.** 6), revealing the reduced impact of stiffness on W_{ext} .

4.3. Linking the energy budget to physical properties

Examining the distributions of fault slip, uplift and strain energy density (SED) provides further insights into the differences in energy partitioning between the centimeter-scale and kilometer-scale models with different material properties (**Fig. 8**). Fault slip produces W_{fric} , uplift produces W_{grav} , and the SED produces the internal work, W_{int} , and thus controls W_{ext} . The centimeter-scale and kilometer-scale models with the upper estimates of material properties (E=100 GPa, D_c =10 m) have essentially identical distributions fault slip, uplift and SED. These identical kinematics and SED produce the identical partitioning of the energy budget in both the centimeter- and kilometer-scale models (**Figs.** S2, 6-7).

In contrast, the kilometer-scale models with the lower estimates of material properties $(p=p_0l^{0.8})$ have kinematics and SED that differ from the centimeter-scale model, and correspondingly. the kilometer-scale models with the upper estimates of material properties $(p=p_0l^1)$. Preceding thrusting, slip along the detachment drops to near zero at 35 km from the backwall in the kilometer-scale model with $p=p_0l^{0.8}$, whereas the normalized slip is near 0.4 at 35 cm from the backwall in the centimeterscale model (Fig. 8). The highest magnitudes of uplift occur near the backwall and outboard of the surface slope inflection in the centimeter-scale model where the material ahead of the wedge compacts. The kilometer-scale model with $p=p_0l^{0.8}$, produces little relative uplift outboard of the surface slope inflection, suggesting lesser compaction ahead of the wedge. In the centimeter-scale model, the highest magnitudes of SED develop outboard of the inflection. In the kilometer-scale model, the highest magnitudes of SED develop at the lower left corner of the model, where the detachment meets the backwall. These three metrics are related

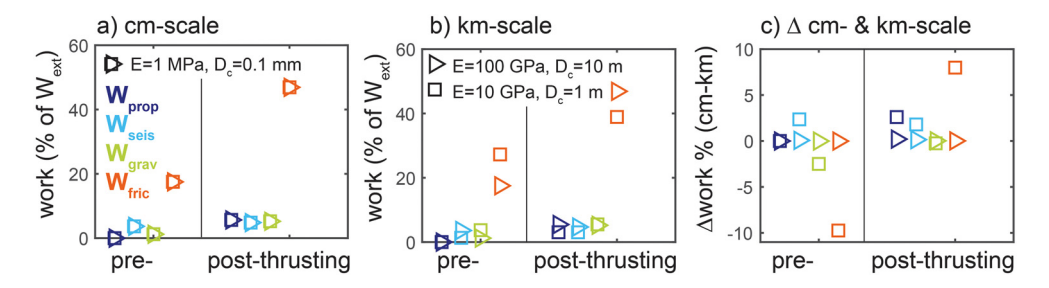


Fig. 7. The partitioning of the energy budget at the centimeter (a) and kilometer (b) scales, and the differences between these scales (c) both pre- and post-thrusting. b) Partitioning of the budget for kilometer-scale models using the upper (triangles) and lower (squares) estimates of the crustal material properties. Using different sets of material properties produce the largest differences in the W_{fric}/W_{ext} calculated at the centimeter- and kilometer-scale, and differences <3% in the other components.

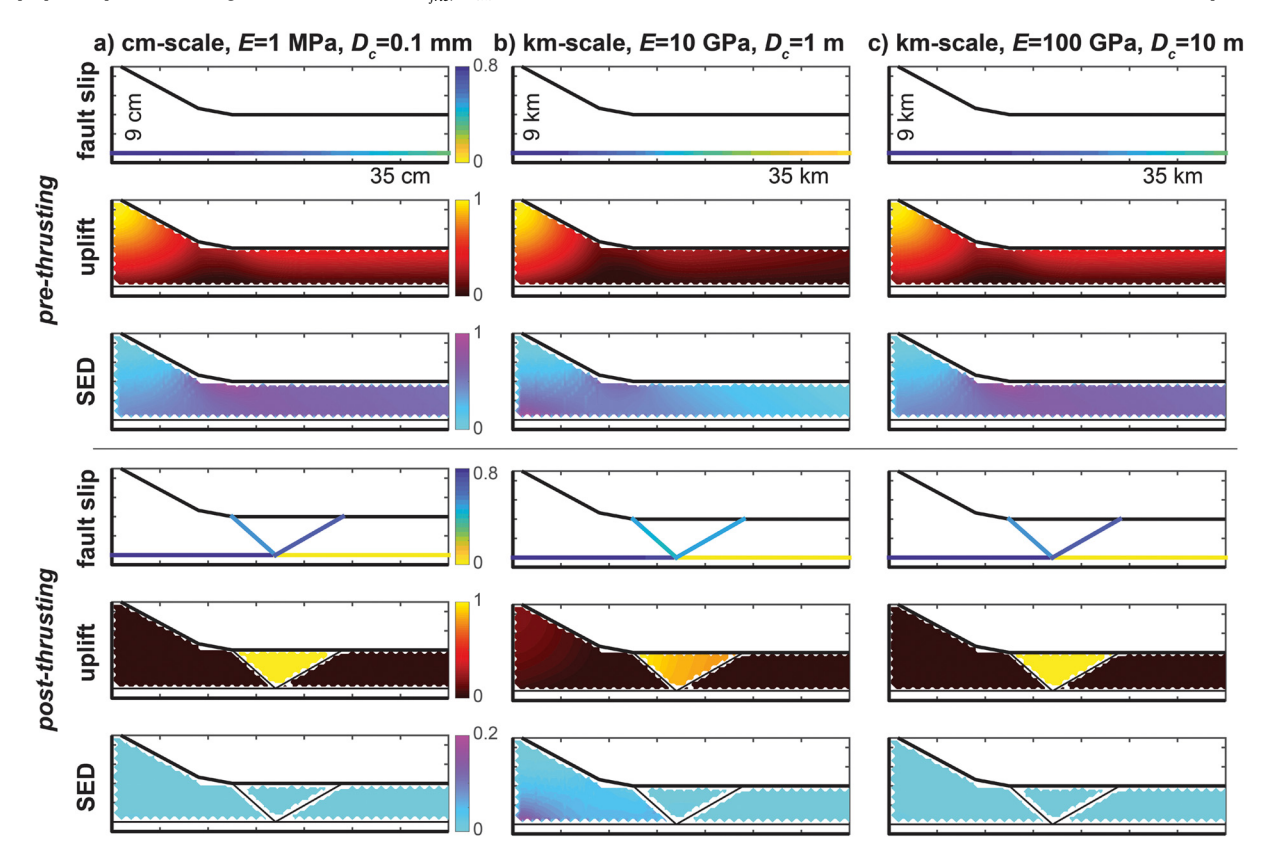


Fig. 8. Physical properties that contribute to the energy budget components in centimeter (a), and kilometer scale wedges (b-c) with lower (b) and upper (c) estimates of crustal material properties. Rows 1-3): Wedges preceding thrust fault development. Rows 4-6): Wedges following thrust fault development. Rows 1, 4): Fault slip produces W_{fric} . Rows 2, 5): Uplift produces W_{grav} . Rows 3, 6): Strain energy density (SED) produces W_{int} and W_{ext} . Each property is normalized by the maximum value within each model in order to aid comparison between models at different scales. The spatial distribution of properties in the wedges in (a) and (c) are virtually identical, while the wedges in (b) show differences in the fault slip, uplift, and SED distributions between those distributions in the wedges in (a) and (c).

because lesser slip on the detachment in front of the wedge may reduce compaction, internal deformation and uplift of the material.

Following thrusting, the forethrust hosts more slip than the backthrust in both the centimeter- and the kilometer-scale model with the upper estimates of material scaling (**Fig.** 8 a, c). In the kilometer-scale model with the lower estimates of material scaling ($p=p_0l^{0.8}$), the backthrust and forethrust host similar magnitudes of slip, and both faults have lesser slip than the thrusts in the centimeter-scale models (**Fig.** 8b). The highest magnitudes of uplift develop uniformly in the triangle of material between the thrust faults in both the centimeter- and kilometer-scale models with higher material scaling (**Fig.** 8a, c). In the kilometer-scale model with lower material scaling (**Fig.** 8b), higher uplift occurs near the backthrust than near the forethrust. The greater relative slip on the backthrust compared to the forethrust yields greater uplift near the backthrust, and rotation of the pop-up between the thrusts. The normalized uplift that occurs in the kilometer-scale

model with lower material scaling is generally 0.8, whereas the triangular zone hosts normalized uplift near 1, or the maximum uplift. The SED field in the kilometer-scale model with lower material scaling shows a concentration of relatively high values near the backwall and detachment intersection (**Fig.** 8b). In contrast, the SED field of both the centimeter- and kilometer-scale model with higher material scaling is uniformly low, and does not host this concentration (**Fig.** 8 a, c).

These patterns of normalized fault slip, uplift and SED reveal the sensitivity of the system's kinematics to differences in the material properties. The distributions are nearly identical in the centimeter-scale models and kilometer-scale models when the material properties scale with exponent of one, highlighting the importance of appropriately scaling the material properties in physical experiments to approximate the crustal values. The energy budget framework concisely quantifies the similarities and differences between the expressions of these physical properties. Moreover,

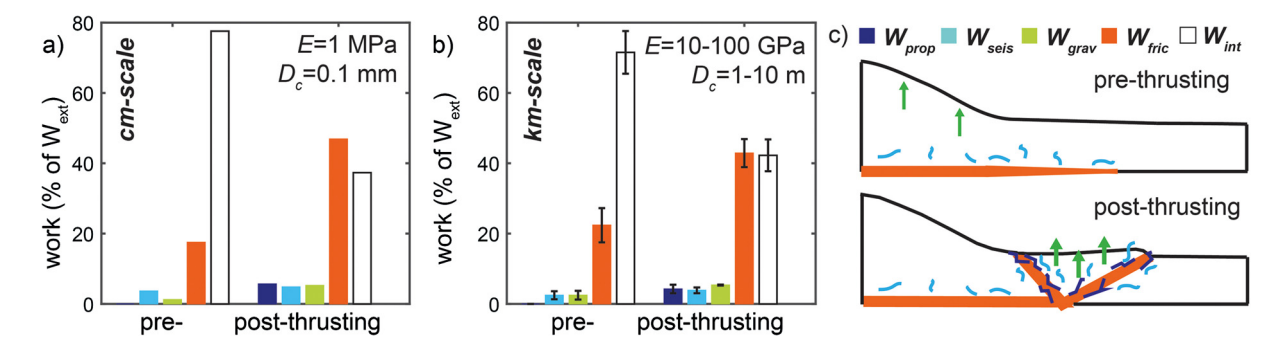


Fig. 9. Energy budget of the centimeter (a) and kilometer (b) scale wedges pre- and post-thrusting as proportions of the overall external work, W_{ext} , and as schematic representations (c). Balancing the energy budget produces the estimates of the internal work, W_{int} . When the crustal wedge has the upper estimates of the material properties (E=100 GPa, D_c =10 m), the partitioning at the crustal scale matches the partitioning at the centimeter scale. Preceding thrusting, $W_{int} > W_{fric}$ at both length scales. Following thrusting at the centimeter scale, assuming the lower estimates of crustal material properties (E=10 GPa, D_c =1 m), $W_{int} > W_{fric}$. If the crustal material properties are within the range of E=10-100 GPa, and D_c =1-10 m, then $W_{int} \approx W_{fric}$. O) The green arrows represent the uplift within the wedge, and the contribution to W_{grav} . The orange lines represent the slip on the faults, and thus the contribution to W_{fric} . The light and dark blue curves represent the stress drop on the faults that occurs when slip is greater and less than the slip weakening distance, and thus the contribution of W_{seis} and W_{prop} , respectively.

these observed differences in the kilometer-scale models with different ranges of material properties highlight the differences that arise only from varying the material properties, rather than from both the material properties and length scale.

5. Discussion

5.1. Energy budget partitioning in accretionary wedges

The partitioning of the energy budget observed in the laboratory-scale numerical models matches the partitioning calculated in the physical experiments upon which the models are based (McBeck et al., 2018). In both of these systems, following thrust fault development, frictional work consumes one of the largest calculated portions of the energy budget (40-50%) (**Fig.** 9). Although we do not directly calculate W_{int} in the present accretion models, following the conservation of energy theory, $W_{int} = W_{ext} - (W_{prop} + W_{seis} + W_{fric} + W_{grav})$. Using the ranges of work estimates from the centimeter-scale models and kilometer-scale models with different material properties, W_{fric} is about equal to W_{int} following thrusting, and each represent 40-50% of W_{ext} .

This partitioning of the energy budget is similar to those in previous numerical models of accretionary sandbox experiments with thrust faults at later stages of wedge development than modeled here (Del Castello and Cooke, 2007). Del Castello and Cooke (2007) calculated components of the energy budget in numerical models with larger overburden thickness relative to the sandpack thickness, higher stiffnesses (13 MPa), longer lengths (1 m), and detachment faults with higher friction coefficients (0.7) than the laboratory-scale wedges modeled here. Throughout cycles of underthrusting and accretion, these wedges host energy budget partitioning with $W_{fric} \approx W_{int} > W_{grav}$. This partitioning agrees with estimates from kinematic models of the Taiwan wedge, in which $W_{fric} \approx 60\%$, 25% is dissipated against internal friction, and $W_{grav} \approx 15\%$ (Dahlen and Barr, 1989). This partitioning disagrees with more recent estimates of the Taiwan wedge: $W_{int} \approx 54\%$, $W_{grav} \approx 35\%$, $W_{fric} \approx 11\%$ (Meade, 2013), perhaps due to this analysis considering the influence of pore pressure. Considering pore pressure in the energy budget calculations can decrease W_{fric} , thereby increasing W_{int} when it is estimated from W_{ext} , as done by Meade (2013).

The numerical estimations of W_{int}/W_{ext} found in the present work and in Del Castello and Cooke (2007) are higher than that of estimates calculated directly from displacement fields of the physical accretionary experiments (McBeck et al., 2018). These higher estimates may arise from the linear elastic material properties of the numerical wedges and the lack of off-fault, distributed

failure and associated plastic dissipative energy in the numerical models. The assumption of linear elasticity leads to higher stresses developing within the bulk wedge material, and consequently against the backwall, than would develop if we numerically modeled the system with discrete granular aggregates, for example. These higher normal stresses against the backwall lead to higher estimates of W_{ext} , and correspondingly W_{int} . This effect is more significant in models preceding thrust fault development. Preceding thrust fault development, W_{int}/W_{ext} (67-77%) is larger than W_{fric}/W_{ext} (17-27%) in both the centimeter- and kilometer-scale models. W_{int} consumes a larger portion of W_{ext} preceding thrust fault development because the influence of the elastic parameters on W_{int} is amplified when the wedge lacks thrust faults.

The dominance of W_{fric} and W_{int} in the energy budget suggests that these components may reflect the overall energetic efficiency of a tectonic system. Previous numerical studies suggest that assessing the external work of an evolving fault network provides accurate predictions of the evolving geometry of this network (e.g., McBeck et al., 2016, 2017a, 2017b; Madden et al., 2017). So, the dominance of W_{fric} and W_{int} in the energy budget at both the crustal and laboratory scale suggests that we may use these components to predict the geometry of propagating, interacting and linking fault networks. This suggestion is a powerful conclusion because constraining W_{fric} and, to a lesser extent W_{int} , in crustal tectonic systems is less hindered by uncertainty than estimating the total external work.

5.2. Scaling the energy budget

Each component of the energy budget scales approximately as power-laws with exponents of three over five orders of magnitude of length scale using the upper and lower estimates of the crustal material properties (Fig. 6). If the numerical models were 3D, instead of 2D plane strain systems, the power-law exponent of three may arise only from the expected volume increase. In 3D systems, increasing the dimensions of the models are expected to increase the volume by a power of three. However, because the models are 2D, increasing the dimensions does not lead to an increase to the third power, but only to the second power (e.g., Figure S3). In particular, the relationships between the length scale and each work component divided by the model volume (cross sectional area multiplied by 1 m) form power laws with exponents of one (Figure S3). This remaining power law exponent of one, after removing the influence of volume, arises from how the effective stiffness influences the stress tensor. Following Hubbert (1937), scaling the elastic modulus is equivalent to scaling the axial stress when the axial strain at the laboratory and crustal scale are equal

(**Text** S4). In summary, the increase in the elastic modulus effectively scales the stress, and so contributes to 1/3 of the exponent, and the increase in the model volume contributes to 2/3 of the power-law exponent of three (e.g., **Figure** S3).

The power law scaling of the work budget components depends on the scaling of the material properties. When the effective Young's modulus and slip weakening distance scale as power laws with an exponent of one relative to the length scale, $p=p_0l^1$, the partitioning of the energy budget is identical from the centimeterto kilometer-scale wedges (**Fig.** 6). When the material properties scale as power laws with exponents less than one, $p=p_0l^{0.8}$, the partitioning is not constant across these length scales (**Figure** S2). As the proportion of W_{ext} consumed by each component differs from the laboratory to crustal scale, W_{fric} and W_{int} continue to dominate the budget, consuming higher portions than the other components.

The post-thrusting simulations represent well-developed crustal wedges more accurately than the pre-thrusting simulations, so we focus on the crustal implications of the energy budget partitioning in the post-thrusting wedges in this discussion. In wedges with active thrust faults, if $p = p_0 l^{0.8}$, laboratory-scale wedges produce relatively less W_{int} and more W_{fric} out of the total available W_{ext} than crustal-scale wedges. Alternatively, if $p = p_0 l^1$, the energy budget partitioning is identical at the laboratory and crustal scales.

Overall, the ranges in the energy budget components produced by assuming these upper and lower estimates of crustal properties are <10% for each component, producing broadly similar energy budget partitioning at the laboratory and crustal scales. This similarity supports the conclusion that the energy budget partitioning measured in the laboratory is similar to the energy budget partitioning in crustal accretionary wedges, provided that both systems have similar fault geometries and surface topographies.

6. Conclusions

Using scaled analog accretion laboratory experiments to develop numerical models, we analyze the partitioning of the energy budget in numerical models that vary over five orders of magnitude in length scale, from the laboratory to crust. The partitioning of the energy budget of accretionary wedges at the laboratory scale matches that at the crustal scale with frictional work dominating the energy budget (40-50% of the total work) after accretionary thrust faults form (Fig. 9), consistent with previous work (e.g., Madden et al., 2017; McBeck et al., 2018, 2019; Aben et al., 2019; Okubo et al., 2019). This result suggests that measurements of the frictional work consumed in a tectonic system may adequately reflect the overall efficiency of a system that includes throughgoing active faults. However, internal work also comprises a nonnegligible portion of the overall efficiency in these models (40-50%). Robust estimates of the total efficiency of tectonic systems may require constraining both the frictional and internal work. More generally, the relative ranking of the energy budget following thrust fault development, $W_{int} \approx W_{fric} >> W_{grav} \approx W_{prop} \approx W_{seis}$, is independent of the length scale or range of tested material properties.

Declaration of competing interest

The authors declare that they have no known competing financial interests or personal relationships that could have appeared to influence the work reported in this paper.

Acknowledgements

This work was supported by a Geological Society of America Student Research Grant and an International Association of Mathematical Geologists Student Research Grant to JM, a National Science Foundation grant EAR-1650368 to MC and a Norwegian Research Council grant 267775 to FR. We thank Fabian Barras, Betsy Madden, Editor Rebecca Bendick, and two anonymous reviewers for suggestions that improved the manuscript.

Appendix A. Supplementary material

Supplementary material related to this article can be found online at https://doi.org/10.1016/j.epsl.2020.116276.

References

- Aben, F.M., Brantut, N., Mitchell, T.M., David, E.C., 2019. Rupture energetics in crustal rock from laboratory-scale seismic tomography. Geophys. Res. Lett. 46 (13), 7337–7344.
- Abercrombie, R., Rice, J.R., 2005. Can observations of earthquake scaling constrain slip weakening? Geophys. J. Int. 162, 406–424.
- Bieniawski, Z.T., 1984. Rock Mechanics Design in Mining and Tunnelling. A.A. Balkema, The Netherlands.
- Cocco, M., Bizzarri, A., 2002. On the slip-weakening behavior of rate- and state dependent constitutive laws. Geophys. Res. Lett. 29 (11), 11-1.
- Cocco, M., Tinti, E., 2008. Scale dependence in the dynamics of earthquake propagation: evidence from seismological and geological observations. Earth Planet. Sci. Lett. 273 (1–2), 123–131.
- Coffey, G.L., Savage, H.M., Polissar, P.J., Rowe, C.D., Rabinowitz, H.S., 2019. Hot on the trail: coseismic heating on a localized structure along the Muddy Mountain fault, Nevada, J. Struct. Geol. 120, 67–79.
- Cooke, M.L., Madden, E.H., 2014. Is the Earth lazy? A review of work minimization in fault evolution. J. Struct. Geol. 66, 334–346. https://doi.org/10.1016/j.jsg.2014.
- Cooke, M.L., Pollard, D.D., 1997. Bedding plane slip in initial stages of fault-related folding. J. Struct. Geol. 19, 567–581.
- Dahlen, F.A., Barr, T.D., 1989. Brittle frictional mountain building: 1. Deformation and mechanical energy budget. J. Geophys. Res., Solid Earth 94 (B4), 3906–3922.
- Del Castello, M., Cooke, M.L., 2007. Underthrusting-accretion cycle: work budget as revealed by the boundary element method. J. Geophys. Res., Solid Earth 112 (B12).
- Di Toro, G., Goldsby, D.L., Tullis, T.E., 2004. Friction falls towards zero in quartz rock as slip velocity approaches seismic rates. Nature 427, 436–439.
- Dieterich, J.H., 1981. Constitutive properties of faults with simulated gouge. In: Carter, N.L., et al. (Eds.), Mechanical Behavior of Crustal Rocks. In: Geophysical Monograph Series, vol. 24. AGU, Washington, D. C., pp. 102–120.
- Fjær, E., Nes, O.M., 2014. The impact of heterogeneity on the anisotropic strength of an outcrop shale. Rock Mech. Rock Eng. 47 (5), 1603–1611.
- Fulton, P.M., Brodsky, E.E., Kano, Y., Mori, J., Chester, F., Ishikawa, T., Harris, R., Lin, W., Eguchi, N., Toczko, S., 2013, Expedition 343, 343T, and KR13-08 Scientists. Low coseismic friction on the Tohoku-Oki fault determined from temperature measurements. Science 342 (6163), 1214–1217.
- Guatteri, M., Spudich, P., Beroza, G., 2001. Inferring rate and state friction parameters from a rupture model of the 1995 Hygo-ken Nanbu (Kobe) Japan earthquake. J. Geophys. Res., Solid Earth 106 (B11), 26511–26521.
- Hardy, S., Finch, E., 2006. Discrete element modelling of the influence of cover strength on basement-involved fault-propagation folding. Tectonophysics 415 (1-4), 225-238.
- Herbert, J.W., Cooke, M., Souloumiac, P., Madden, E., Mary, B.C., Maillot, B., 2015. The work of fault growth in laboratory sandbox experiments. Earth Planet. Sci. Lett. 432, 95–102.
- Hirose, T., Bystricky, M., 2007. Extreme dynamic weakening of faults during dehydration by coseismic shear heating. Geophys. Res. Lett. 34 (14), L14311. https://doi.org/10.1029/2007GL030049.
- Hubbert, M.K., 1937. Theory of scale models as applied to the study of geologic structures. Bull. Geol. Soc. Am. 48 (10), 1459–1520.
- Ismat, Z., 2009. Energy budget during fold tightening of a multilayer fold. J. Struct. Geol. 31 (9), 972–988.
- Kanamori, H., Heaton, T.H., 2000. Microscopic and macroscopic physics of earthquakes. In: Geophysical Monograph, vol. 120. American Geophysical Union, pp. 147–164.
- Klinkmüller, M., Schreurs, G., Rosenau, M., Kemnitz, H., 2016. Properties of granular analogue model materials: a community wide survey. Tectonophysics 684, 23–38.
- Lohrmann, J., Kukowski, N., Adam, J., Oncken, O., 2003. The impact of analogue material properties on the geometry, kinematics, and dynamics of convergent sand wedges. J. Struct. Geol. 25, 1691–1711. https://doi.org/10.1016/S0191-8141(03) 00005-1.
- Madden, E.H., Cooke, M.L., McBeck, J., 2017. Energy budget and propagation of faults via shearing and opening using work optimization. J. Geophys. Res., Solid Earth 122 (8), 6757–6772.

- Maillot, B., 2013. A sedimentation device to produce uniform sand packs. Tectonophysics 593, 85–94. https://doi.org/10.1016/j.tecto.2013.02.028.
- Marone, C., Kilgore, B., 1993. Scaling of the critical slip distance for seismic faulting with shear strain in fault zones. Nature 362, 618–621.
- Meade, B.J., 2013. Revisiting the orogenic energy balance in the western Taiwan orogen with weak faults. Terra Nova 25 (2), 160–164.
- McBeck, J., Madden, E., Cooke, M., 2016. Growth by Optimization of Work (GROW): a new modeling tool that predicts fault growth through work minimization. Comput. Geosci. 88, 142–151.
- McBeck, J.A., Cooke, M.L., Herbert, J.W., Maillot, B., Souloumiac, P., 2017a. Work optimization predicts accretionary faulting: an integration of physical and numerical experiments. J. Geophys. Res., Solid Earth 122 (9), 7485–7505.
- McBeck, J., Cooke, M., Madden, E., 2017b. Work optimization predicts the evolution of extensional step overs within anisotropic host rock: Implications for the San Pablo Bay, CA. Tectonics 36 (11), 2630–2646.
- McBeck, J.A., Cooke, M.L., Souloumiac, P., Maillot, B., Mary, B., 2018. The influence of detachment strength on the evolving deformational energy budget of physical accretionary prisms. Solid Earth 9, 1421–1436. https://doi.org/10.5194/se-9-1421-2018
- McBeck, J., Cordonnier, B., Mair, K., Renard, F., 2019. The evolving energy budget of experimental faults within continental crust: Insights from in situ dynamic X-ray microtomography. J. Struct. Geol. 123, 42–53.
- Mikumo, T., Olsen, K.B., Fukuyama, E., Yagi, Y., 2003. Stress-breakdown time and slip-weakening distance inferred from slip-velocity functions on earthquake faults. Bull. Seismol. Soc. Am. 93 (1), 264–282.
- Mondol, N.H., Bjørlykke, K., Jahren, J., Høeg, K., 2007. Experimental mechanical compaction of clay mineral aggregates—changes in physical properties of mudstones during burial. Mar. Pet. Geol. 24 (5), 289–311.
- Ohnaka, M., 2000. A physical scaling relation between the size of an earthquake and its nucleation zone size. Pure Appl. Geophys. 157, 2259–2282.
- Ohnaka, M., Kuwahara, Y., 1990. Characteristic features of local breakdown near a crack-tip in the transition zone from nucleation to unstable rupture during stick-slip shear failure. Tectonophysics 175, 197–220.
- Okubo, K., Bhat, H.S., Rougier, E., Marty, S., Schubnel, A., Lei, Z., Knight, E., Klinger, Y., 2019. Dynamics, radiation and overall energy budget of earthquake rupture with coseismic off-fault damage. arXiv preprint. arXiv:1901.01771.

- Panien, M., Schreurs, G., Pfiffner, A., 2006. Mechanical behaviour of granular materials used in analogue modelling: insights from grain characterisation, ring-shear tests and analogue experiments. J. Struct. Geol. 28 (9), 1710–1724.
- Passelègue, F., Schubnel, A., Nielsen, S., Bhat, H.S., Deldicque, D., Madariaga, R., 2016. Dynamic rupture processes inferred from laboratory microearthquakes. J. Geophys. Res., Solid Earth 121 (6), 4343–4365.
- Pulido, N., Irikura, K., 2000. Estimation of dynamic rupture parameters from the radiated seismic energy and apparent stress. Geophys. Res. Lett. 27 (23), 3945–3948.
- Raimbourg, H., Hamano, Y., Saito, S., Kinoshita, M., Kopf, A., 2011. Acoustic and mechanical properties of Nankai accretionary prism core samples. Geochem. Geophys. Geosyst. 12 (4). https://doi.org/10.1029/2010GC003169.
- Reber, J.E., Cooke, M.L., Dooley, T.P., 2020. What model material to use? A review on rock analogs for structural geology and tectonics. Earth-Sci. Rev., 103107.
- Ritter, M.C., Leever, K., Rosenau, M., Oncken, O., 2016. Scaling the sandbox—mechanical (dis) similarities of granular materials and brittle rock. J. Geophys. Res., Solid Earth 121 (9), 6863–6879.
- Savage, H.M., Cooke, M.L., 2010. Unlocking the effects of friction on fault damage zones. J. Struct. Geol. 32 (11), 1732–1741.
- Savage, H.M., Polissar, P.J., Sheppard, R., Rowe, C.D., Brodsky, E.E., 2014. Biomarkers heat up during earthquakes: new evidence of seismic slip in the rock record. Geology 42 (2), 99–102.
- Sone, H., Zoback, M.D., 2013. Mechanical properties of shale-gas reservoir rocks— Part 1: static and dynamic elastic properties and anisotropy. Geophysics 78 (5), D381–D392.
- Spinelli, G.A., Mozley, P.S., Tobin, H.J., Underwood, M.B., Hoffman, N.W., Bellew, G.M., 2007. Diagenesis, sediment strength, and pore collapse in sediment approaching the Nankai Trough subduction zone. Geol. Soc. Am. Bull. 119 (3–4), 377–390.
- Strasser, M., Moore, G.F., Kimura, G., Kitamura, Y., Kopf, A.J., Lallemant, S., Park, J., Screaton, E., Su, X., Underwood, M., Zhao, X., 2009. Origin and evolution of a splay fault in the Nankai accretionary wedge. Nat. Geosci. 2 (9), 648. https://doi.org/10.1038/NGE0609.
- Tinti, E., Cocco, M., Fukuyama, E., Piatanesi, A., 2009. Dependence of slip weakening distance (Dc) on final slip during dynamic rupture of earthquakes. Geophys. J. Int. 177 (3), 1205–1220.